www.nature.com/scientificreports

scientific reports

OPEN

Radiation-resistant C-type dipole dump magnet for MIR/THz FEL applications at TARLA

Kubilay Bayramoglu[1], Fedai İnanır[2,7], Zuhal Oktay[3,7]✉, Can Coskun[4,7], Sükrü Yıldız[5], Özgür Akcalı[2], Memet Yılmaz[2] & Haris Dapo[6]

Radiation-induced degradation is a key challenge for dipole magnets used in beam dump systems of free-electron laser (FEL) facilities. This study presents the design and experimental validation of a compact, radiation-resistant C-type dipole dump magnet developed for the MIR/THz FEL at the Turkish Accelerator and Radiation Laboratory (TARLA). The magnet deflects electron beams of up to 45 MeV by 42°, enabling safe beam disposal under radiation-intensive conditions. A radiation-informed design approach combining magnetic material characterization, electromagnetic modeling, and Monte Carlo radiation transport simulations was employed. Electrical steel with high iron content was selected to ensure sufficient saturation margin and magnetic stability in the fringe-field-dominated geometry. Coupled MCNP–COMSOL analyses showed that the combined radiation and resistive heating leads to a maximum coil temperature rise of only 18.7 °C, allowing reliable air-cooled operation. A parallel winding scheme was adopted to reduce Joule losses and enhance thermal margins. Neutron shielding experiments using a locally developed composite material achieved up to 99% attenuation, confirming the effectiveness of the shielding design. The proposed magnet provides a compact and radiation-tolerant solution for FEL beam dump systems.

Keywords Radiation-resistant dipole magnet, C-type beam dump magnet, Neutron shielding, Monte Carlo radiation transport, Electromagnetic–thermal coupling

Radiation-resistant dipole magnets are essential for accelerator regions exposed to intense secondary radiation, such as beam dumps and target areas. Facilities including the Hadron Experimental Hall of the Japan Proton Accelerator Research Complex (J-PARC)[1], the Super-FRS at GSI[2,3], and the High-Luminosity LHC[7] require magnet systems capable of maintaining stable beam control under severe radiation and thermal loads. In these environments, radiation-induced degradation of magnetic, electrical, and mechanical properties can significantly affect magnet lifetime and operational reliability.

To mitigate these effects, existing radiation-tolerant magnet systems often employ high-temperature superconductors, radiation-hard insulation materials, and mechanically reinforced cooling structures[4–6]. While such solutions provide high field capability and improved radiation tolerance, they typically rely on cryogenic systems, water cooling, and complex mechanical assemblies, which increase system complexity, maintenance requirements, and vulnerability in radiation-rich environments[6,7].

Beam dump systems play a critical role in safely dissipating particle beam energy during routine operation and emergency shutdowns, and dipole magnets are commonly used to steer the beam toward dedicated absorbers[8,9]. In large-scale facilities such as the Rare Isotope Accelerator and the Large Hadron Collider, dump magnets are designed for very high beam power and therefore incorporate laminated steel yokes, internal cooling channels, or cryogenic infrastructure to manage extreme thermal loads[9–12]. Although high-temperature superconducting magnets can provide higher magnetic fields, their operation introduces additional challenges related to cryogenic stability and radiation-induced disturbances such as flux jumps[13].

[1]Department of Mechanical Engineering, Zonguldak Bülent Ecevit University, 67100 Zonguldak, Turkey. [2]Department of Physics, Faculty of Arts and Sciences, Yıldız Technical University, Istanbul, Turkey. [3]Department of Advanced Energy Technologies, Institute of Clean Energy Technologies, Yıldız Technical University, Istanbul, Turkey. [4]Department of Mechanical Engineering, Yıldız Technical University, Istanbul, Turkey. [5]Faculty of Engineering and Architecture, Department of Metallurgy and Materials Engineering, Kırşehir Ahi Evran University, Kirşehir, Turkey. [6]Turkish Accelerator and Radiation Laboratory, Ankara, Turkey. [7]Superconducting Cable Industry Inc, Istanbul, Turkey. ✉email: z.oktay@yildiz.edu.tr

In contrast, MIR/THz free-electron laser facilities operate at moderate beam energies but experience continuous radiation exposure in compact geometries, making long-term robustness and operational simplicity more critical than maximum field strength. Most reported dump magnet designs are optimized for high-energy accelerators and rely on water-cooled, laminated-steel structures, which are not ideal for radiation-tolerant and low-maintenance FEL beam dumps.

The present work addresses this gap by developing a radiation-resistant, air-cooled C-type dipole dump magnet optimized for MIR/THz FEL beam dump and spectrometer applications at TARLA. Compared to conventional dump magnets, the proposed design combines radiation-informed material selection—using low-copper, high-iron electrical steel to reduce activation and radiation-induced degradation—with aluminum coils to minimize long-term activation. In addition, the open C-type geometry facilitates localized neutron shielding integration and reduces back-scattered radiation toward the coils, while a widened pole gap and conservative magnetic length margin ensure reliable beam interception under fringe-field and alignment uncertainties. These features distinguish the proposed system from previously reported dump magnet implementations[1–13] and provide a practical, scalable solution for radiation-tolerant beam dumping in compact FEL facilities.

While effective for high-energy accelerators, conventional beam dump magnet designs introduce significant complexity, maintenance requirements, and vulnerability in radiation-rich environments. Radiation-induced material degradation and the reliability of active cooling systems are particularly challenging for compact FEL beam dumps, where beam energies are moderate but radiation exposure is continuous. Most reported designs rely on water-cooled, laminated-steel magnets, which are not well suited for simplified and radiation-tolerant operation.

The present work addresses this gap by developing a radiation-resistant, air-cooled C-type dipole magnet optimized for MIR/THz FEL beam dump and spectrometer applications at TARLA. Unlike high-energy accelerator dump systems, the proposed design prioritizes operational simplicity, air cooling, and radiation-informed material selection, while maintaining reliable beam deflection performance. Compared to conventional dump magnets implemented at existing FEL and accelerator facilities, the proposed C-type dipole dump magnet introduces several design innovations specifically aimed at enhancing radiation robustness. These include the use of low-copper, high-iron electrical steels to improve resistance against radiation-induced embrittlement and conductivity degradation, a widened pole gap combined with a conservative magnetic length margin to ensure reliable beam interception, and an open C-type geometry that facilitates localized shielding integration and reduces neutron backscattering toward the coils. Together, these features distinguish the proposed solution from previously reported dump magnet implementations and make it particularly suitable for high-power MIR/THz FEL beam dumping at TARLA.

Methods

Unlike conventional dump magnets used in FEL and linac facilities, where radiation effects are often treated as secondary constraints, the proposed C-type dump magnet was designed following a radiation-driven methodology. In this approach, radiation robustness was considered simultaneously with magnetic performance from the earliest design stages. The novelty of the present design lies in the combined optimization of magnet geometry, material selection, and shielding configuration to mitigate neutron-induced activation and material degradation. In particular, the coil system was deliberately positioned outside the direct radiation line, while the magnet yoke geometry was optimized to reduce neutron streaming toward sensitive components. This integrated design philosophy distinguishes the proposed dump magnet from previously reported implementations and significantly enhances its long-term operational reliability in high-radiation FEL environments.

Material selection and preparation

More than twenty candidate ferromagnetic materials were initially evaluated for use in the dump magnet yoke, including laminated electrical steels, ferrites, high-saturation alloys, and Armco-type pure irons such as DT4. The selection was based on a multi-criteria methodology incorporating magnetic performance, radiation tolerance, mechanical stability, and manufacturability, reflecting the operational demands of a radiation-exposed FEL beam dump magnet. Primary screening criteria included saturation flux density, coercivity, iron (Fe) fraction, copper (Cu) content, and carbon concentration. A high Fe fraction was required to ensure high saturation magnetization and stable magnetic performance under strong excitation fields. Low Cu content was favored to minimize neutron activation and radiation-induced conductivity degradation, while low carbon levels were selected to reduce radiation-induced embrittlement and mechanical degradation. Materials containing activation-prone elements such as nickel (Ni) and cobalt (Co) were excluded.

Although Armco-type pure irons (DT4) exhibit good radiation tolerance and excellent magnetic softness under ideal conditions, they were not selected for the present compact dipole design for several critical reasons. In practice, DT4 typically exhibits a saturation flux density of only about 1.6 T in rolled and stress-relieved industrial forms, and its coercivity is known to increase significantly after rolling, machining, and mechanical assembly. These effects reduce the effective permeability and narrow the usable linear magnetization range. In compact dipole geometries operating in the 0.45–0.65 T field range, where strong fringe fields and local field enhancements are unavoidable, the available saturation margin becomes an important consideration. Under these conditions, the use of DT4 would reduce the saturation margin in fringe-field-dominated regions, thereby increasing the likelihood of local saturation and field nonlinearity at higher beam energies, particularly near the pole edges and in the return yoke. Such localized effects could lead to reduced field uniformity, increased hysteresis, and lower magnetic stability, which are undesirable for precise and reproducible beam steering. By contrast, modern non-oriented electrical steels provide a higher effective saturation margin, lower hysteresis losses, and superior dimensional and magnetic stability under irradiation. These materials maintain a more linear B–H response in the relevant operating range and are less sensitive to stress-induced magnetic degradation, making them better suited for compact accelerator dipoles.

Ferrites and high-saturation alloys were also evaluated but were not adopted because of either insufficient saturation capability or inferior radiation-induced microstructural stability under the expected neutron and gamma fluxes. In addition to these technical limitations, the relatively higher cost and limited availability of DT4-type Armco iron in the local supply chain further reduced its practical attractiveness. Overall, while DT4 remains an excellent soft-magnetic material for many applications, it was found to be unsuitable for the specific magnetic, mechanical, and radiation-environment requirements of the present compact dipole design.

The elemental compositions and magnetic properties of all candidate materials were characterized using X-ray fluorescence (XRF) and vibrating sample magnetometer (VSM) measurements. Elemental composition analysis was performed using X-ray fluorescence (XRF) spectroscopy. The XRF technique enables non-destructive quantitative determination of elemental composition by measuring characteristic secondary X-rays emitted from the sample under primary X-ray excitation. A detailed description of the XRF methodology and quantitative analysis procedures can be found in Jenkins and De Vries[14]. Among the analyzed samples, Fe was the dominant element (98.56–99.25%), followed by chromium (Cr, 0.39–0.99%), while Cu content ranged from 0.06% to 0.42%. Based on these criteria, six materials were shortlisted as they exhibited superior magnetic stability and radiation tolerance compared with conventional soft steels commonly used in accelerator magnets. Among them, Sample C (electrical steel) was selected for fabrication of the C-type dipole dump magnet due to its optimal combination of high Fe content, low Cu concentration (< 0.1%), low coercivity, and superior radiation resistance, as shown in Fig. 1.

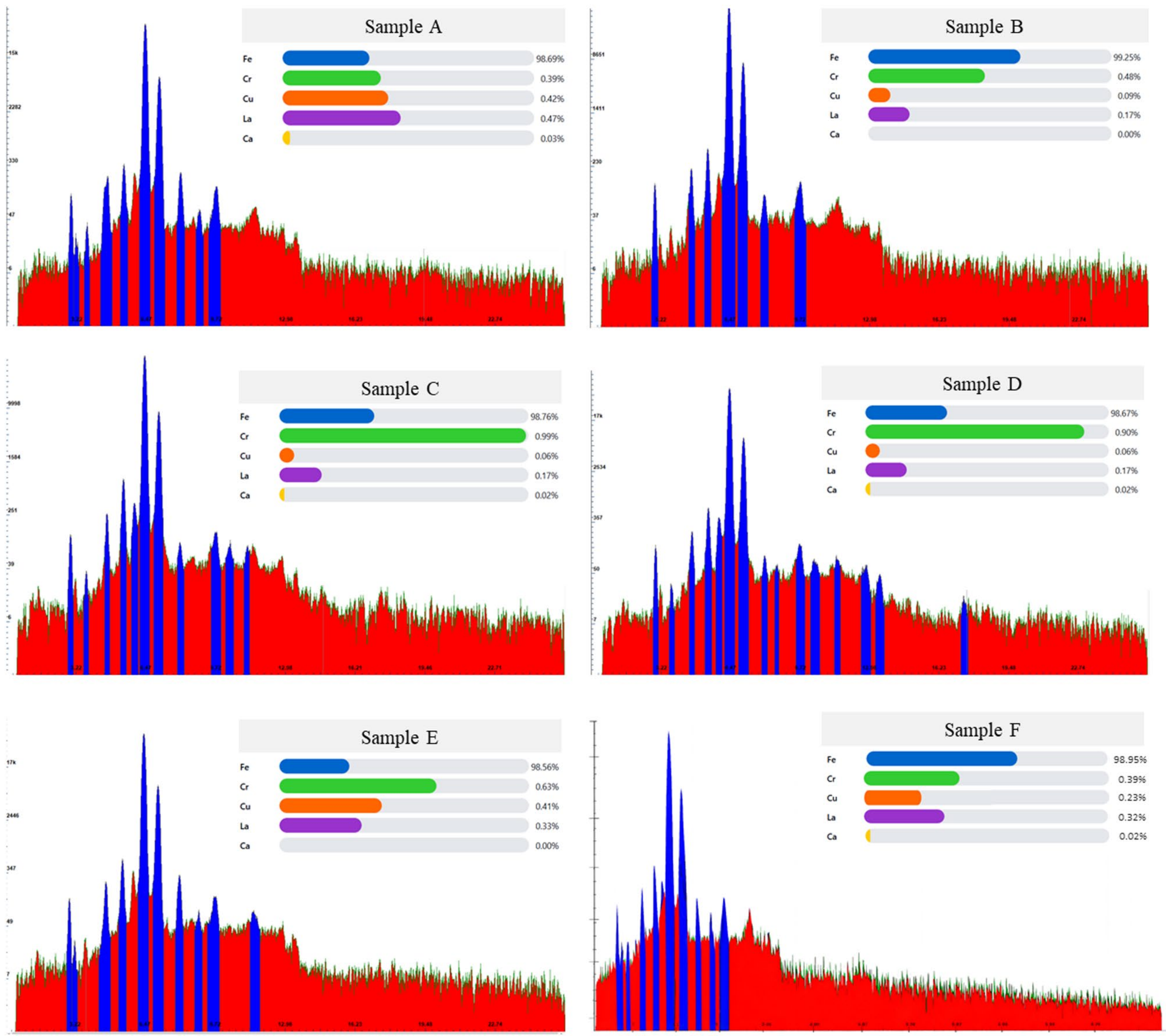

Fig. 1. XRF analysis results of six samples.

Accurate B–H and magnetic permeability curves are essential inputs for obtaining physically meaningful results in multiphysics simulations such as COMSOL Multiphysics, as they define saturation behavior, field linearity, and the operational limits of the magnetic core. In this study, the B–H and permeability curves of the selected electrical steel were experimentally measured using a vibrating sample magnetometer (VSM) at TÜBİTAK-UME and implemented directly in the finite-element model. The VSM system enables precise determination of magnetic hysteresis curves by detecting the magnetic moment induced in a sample that is mechanically vibrated within a uniform applied magnetic field. Typical operational specifications of the system are as follows:

- Magnetic field range: up to ± 1.5 T.
- Field resolution: better than 0.1 mT.
- Moment sensitivity: ~10^{-5} emu.
- Temperature range: 80 K to 800 K.
- Sample size: up to ~ 10 mm in diameter and length.
- Vibration frequency: ~80–100 Hz.
- Measurement mode: DC hysteresis loops.

Measurements were carried out at room temperature under applied fields ranging from − 1.5 T to + 1.5 T. The induced magnetic moment was recorded as a function of the applied magnetic field, and the resulting hysteresis (M–H) curves were used to characterize the magnetic properties of the electrical steel samples. The operating principle and sensitivity of the Vibrating Sample Magnetometer (VSM) technique are described in detail by Foner[15]. The measured magnetization and permeability curves are shown in Fig. 2.

The experimental magnetization data were directly compared with the idealized B–H characteristics provided by the material manufacturer and implemented in the simulations, without applying any post-calibration, scaling, or empirical correction factors. A maximum deviation of approximately 6.28% was observed near magnetic saturation. The deviation was calculated as the relative difference between experimental and simulated magnetization values at the reference field level using:

$$Deviation\ (\%) = \frac{|M_{exp} - M_{sim}|}{M_{exp}} \cdot 100$$

where M_{exp} and M_{sim} represent the experimentally measured and simulated magnetization values, respectively. The comparison therefore reflects intrinsic differences between real material behavior and the idealized assumptions adopted in the numerical model. The observed discrepancy primarily arises from:

1. Microstructural effects: Grain orientation, lamination-induced residual stresses, and manufacturing-related anisotropy present in the measured samples are not fully represented in the isotropic material model used in simulations.

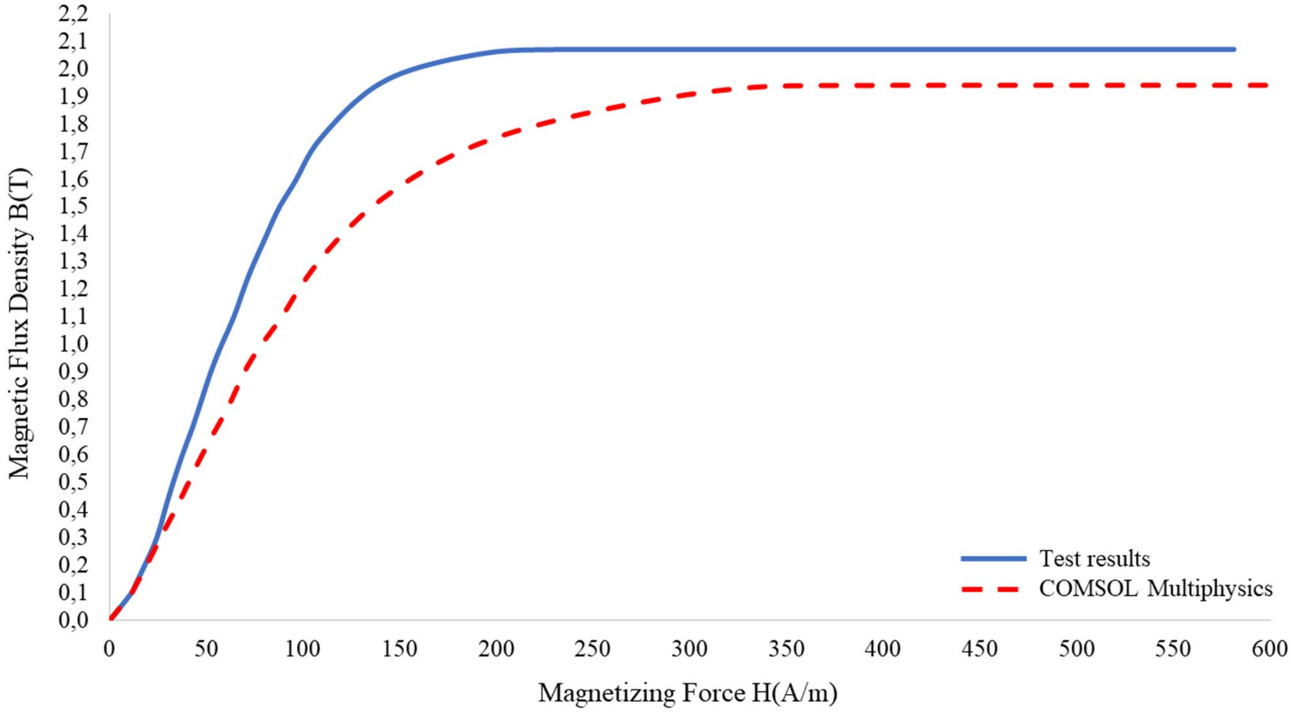

Fig. 2. Magnetization (B–H) and magnetic permeability curves of the selected electrical steel.

2. Compositional tolerances: Minor variations in alloy composition may influence magnetic permeability and saturation characteristics.
3. Measurement conditions: Temperature fluctuations and sample orientation uncertainties during VSM measurements can introduce small deviations.
4. Model idealizations: The numerical model assumes homogeneous and isotropic material properties and neglects local inhomogeneities and edge effects.

Such a deviation (≈ 6%) is consistent with previously reported differences between VSM measurements and numerical models based on manufacturer-provided B–H data, and remains within typical engineering tolerance for electrical steel characterization. Although the dump magnet operates below 0.65 T—where magnetic nonlinearity is relatively moderate—the influence of lamination-induced stresses and potential radiation-related microstructural changes underscores the importance of incorporating experimentally measured material data for reliable lifetime estimation and performance prediction.

Magnet design

The required magnetic field strength of the dump magnet is determined by the beam energy E, bending θ, and effective magnetic length L_{eff} according to

$$B = \frac{p}{q \cdot R} = \frac{E}{0.2998 \cdot R} \tag{1}$$

where the bending radius *R* is related to

$$R = \frac{L_{eff}}{\theta} \tag{2}$$

The bending angle θ can be calculated using the following Eq.

$$\theta = \frac{q \cdot B \cdot L_{eff}}{p} \tag{3}$$

where L_{eff} is the effective magnetic length, q is the electron charge, B is the nominal magnetic field, and p is the electron momentum.

These relations form the basis for selecting the pole gap, excitation current, and magnetic length of the dipole magnet. The electromagnetic framework was established using the Ampère formulation, with Ampère's law serving as the governing equation:

$$\frac{1}{\mu_0 \mu_r} (\nabla \times \nabla \times \boldsymbol{A}) = J \tag{4}$$

where μ_0 denotes the permeability of free space, μ_r the relative permeability, *A* the magnetic vector potential, and *J* the current density, defined as:

$$J = -\sigma \frac{\partial \boldsymbol{A}}{\partial t} + J_s \tag{5}$$

The source current density in the coil is given by $J_s = -\sigma \cdot \nabla \cdot \varphi$, where φ denotes the electric scalar potential. The electrical conductivities of air, copper, and the magnet yoke steel are listed in Eq. (6).

The magnetic field B = ∇×A and the electric field E are related by:

$$\boldsymbol{E} = -\frac{\partial \boldsymbol{A}}{\partial t} - \nabla \phi \tag{6}$$

The Lorentz force was computed using the Magnetic Fields module.

$$\boldsymbol{F_t} = \boldsymbol{e} (\boldsymbol{\nu} \ \boldsymbol{x} \, \boldsymbol{B}) \tag{7}$$

$$\frac{d}{d_t} \left(m_p \frac{dq}{dt} \right) = F_t \tag{8}$$

where q is the particle position vector, $v = \frac{dq}{dt}$ is the particle velocity, and m_p is the relativistic mass of the particle.

The magnet features a 60 mm pole gap designed to deflect electron beams in the energy range of 2–45 MeV by a bending angle of 42°. The core, support structure, and coil assembly are shown in Fig. 3. The magnet is energized by 448-turn rectangular aluminum coils, generating a magnetic flux density in the pole gap ranging from 0.0316 to 0.65 T, depending on the electron energy.

For a 40 MeV electron beam, the magnetic field required to achieve a 42° deflection was calculated to be 0.457 T. As illustrated in Fig. 4, the Turkish Accelerator and Radiation Laboratory (TARLA) has defined a beam deflection angle of 42° as optimal for meeting the facility's radiation protection and operational safety requirements.

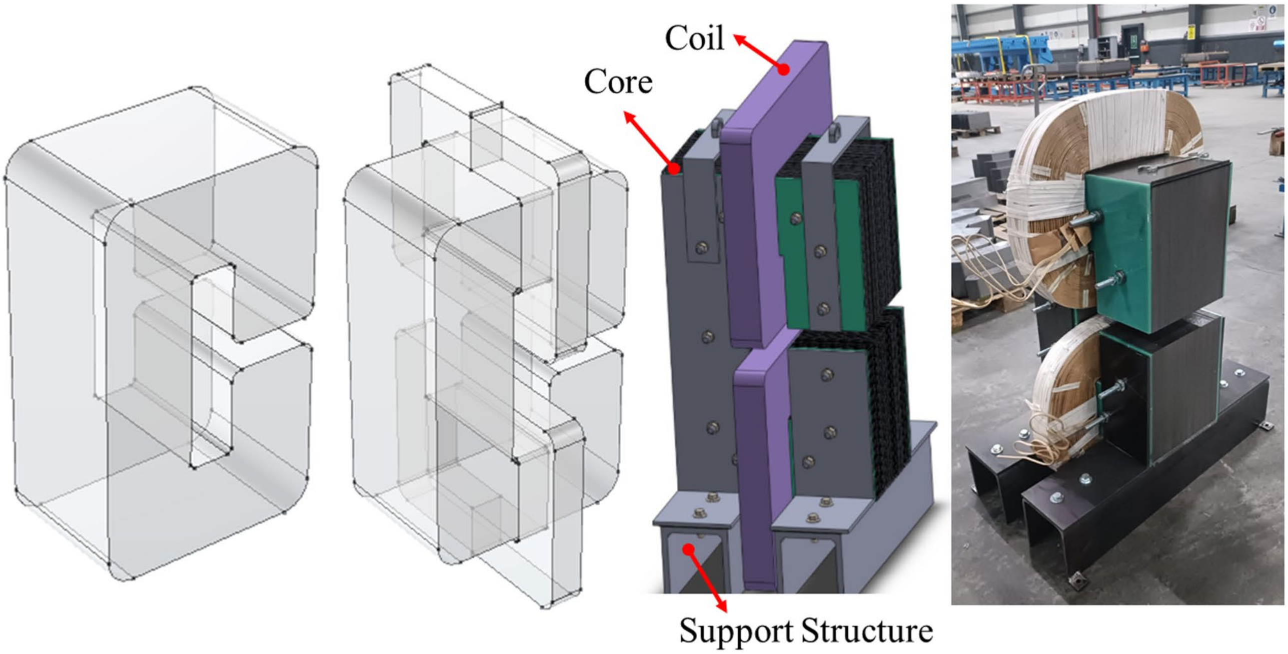

Fig. 3. Technical layout of the C-type dipole dump magnet showing the core, coil assembly, and support structure.

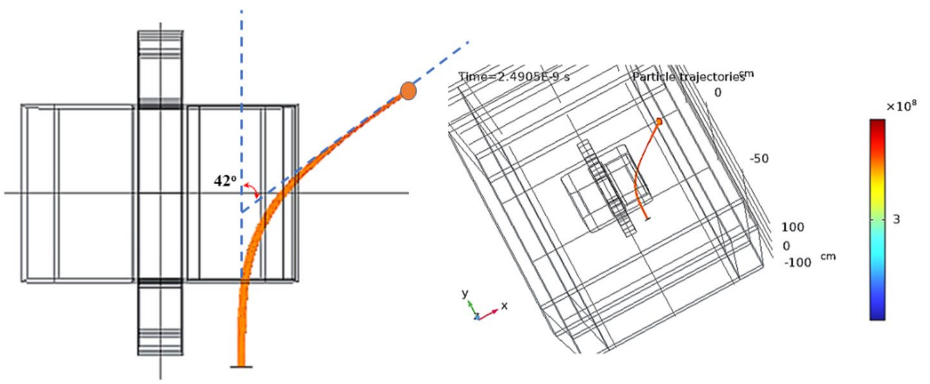

Fig. 4. Simulated electron beam bending angle in the C-type dipole dump magnet as a function of electron energy.

In an ideal dipole magnet, the magnetic field in the gap, B_0, is related to the applied current I by[16]

$$B_0 = \mu_0 \frac{N \cdot I}{h} \tag{9}$$

where N is the number of coil turns, h is the pole gap, and $\mu_0 = 4\pi \times 10^{-7}$ H/m is the permeability of free space. This relation shows that the magnetic field scales linearly with the ampere-turns NIN $N\,I$ and inversely with the pole gap. Based on this expression, a magnetic field of 0.65 T requires approximately 12 kA·turns. For air-cooled coils, a conservative current density of 1.145 A mm^{-2} was selected, resulting in a minimum conductor cross-sectional area of 23.6 mm^2. For air-cooled coils, the maximum allowable current density (J) is typically below 2 A/mm^2[17].

Aluminum conductors were selected for the magnet coils to minimize radiation-induced activation effects. In contrast to copper, which can undergo long-lived radioactive activation under neutron irradiation, aluminum exhibits only short-lived activation and returns to its original state after decay. This material choice significantly reduces long-term radiological hazards and maintenance requirements, thereby extending the operational lifetime of the coils.

The design parameters and initial values used in the magnetic field simulations are summarized in Table 1. The geometrical pole arc length, initially 20 mm, was increased to 32 mm by applying a 60% safety margin. While a margin of approximately 20% is generally sufficient for conventional beam transport magnets, dump

Parameter	Dipole Dump Magnet
Conductor material	Aluminum
Maximum beam energy (MeV)	45
Deflection angle (degrees)	42
Geometrical pole arc length (mm)	32
Magnetic field (T)	0.65
Dipole gap (mm)	60
Maximum current density (A/mm^2)	1.145
Number of coil turns per pole (turns)	448
Coil cross-section area (mm^2)	1976
Current (A)	27.0
Conductor cross-section (mm^2)	23.6
Coil width (mm)	38
Coil height (mm)	52
Active coil length (mm)	320

Table 1. Optimized design parameters of the C-type dipole dump magnet.

magnets must guarantee complete beam interception under beam energy spread, alignment tolerances, fringe-field uncertainties, and potential radiation-induced material degradation. The larger margin adopted here reflects the critical safety function of the dump system and ensures robust, fail-safe operation under all expected operating conditions.

The C-type dipole magnet was designed for DC operation with a 60 mm pole gap and a nominal bending angle of 42° for electrons with kinetic energies between 2 and 45 MeV. The magnet is energized by rectangular aluminum coils with 448 turns per pole.

The coil geometry was constrained by the open C-type yoke, the requirement for localized neutron shielding, and maintenance accessibility. As a result, the turn distribution is asymmetric; however, it was optimized to ensure the required magnetic field strength and uniformity while maintaining compatibility with the integrated shielding and mechanical layout.

The main coil parameters are summarized in Table 1, including the conductor material (aluminum), conductor cross-section (23.6 mm^2), active coil length (320 mm), coil width (38 mm), and coil height (52 mm). The use of aluminum conductors instead of copper provides improved radiation tolerance and reduced long-term activation, which is essential for sustained operation in the radiation environment of the TARLA beam dump system.

Magnetic field simulation and effective length

Although the magnet geometry is symmetric, the three-dimensional magnetic flux density distribution exhibits slight asymmetry due to end effects, coil current routing, and fringe-field leakage. These effects are particularly important for dump magnets because beam deflection depends on the integrated magnetic field along the particle trajectory, especially in the entrance and exit regions, as illustrated in Fig. 5.

The effective magnetic length L_{eff} was calculated using the standard integral definition

$$L_{eff} = \frac{1}{B_0} \int B\left(s\right) ds \tag{10}$$

where $B\left(s\right)$ is the longitudinal magnetic field distribution along the beam axis and B_{center} is the magnetic field at the pole center. The longitudinal field profiles and remote fringe fields were obtained from full three-dimensional FEM simulations.

Figure 5 shows the horizontal magnetic field measured at the center of the pole plates as a function of excitation current, together with COMSOL simulation results. Both datasets exhibit a linear relationship between magnetic field and current, with experimental and numerical values agreeing within 1%, confirming the accuracy of the electromagnetic model in the operating field range. Magnetic field measurements were performed using an FW Bell 5180 Digital Gaussmeter (DC accuracy: ±0.5% of reading; AC accuracy: ±1% of reading; resolution: 0.01 mT). The corresponding magnetic field map for 40 MeV operation is presented in Fig. 6. Based on 240 measurement points, the average magnetic field at 40 MeV was 0.45431 T with a sample standard deviation of ± 0.00105 T. The minimum and maximum measured values were 0.4511 T and 0.4580 T, respectively, indicating good field uniformity across the mapped region.

Although the magnet is geometrically symmetric, the magnetic flux density shows an apparent asymmetry near the magnet ends due to three-dimensional fringe fields and local flux leakage. By integrating the simulated longitudinal field distribution, the effective magnetic length was determined to be L_{eff}=171.1 mm, consistent with the expected influence of end fields on beam deflection. Because the effective magnetic length is more than five times larger than the geometrical pole length (32 mm), more than 80% of the integrated bending field is provided by fringe fields. This makes the magnet particularly sensitive to material saturation and stress-induced permeability changes, which justifies the stringent material selection criteria.

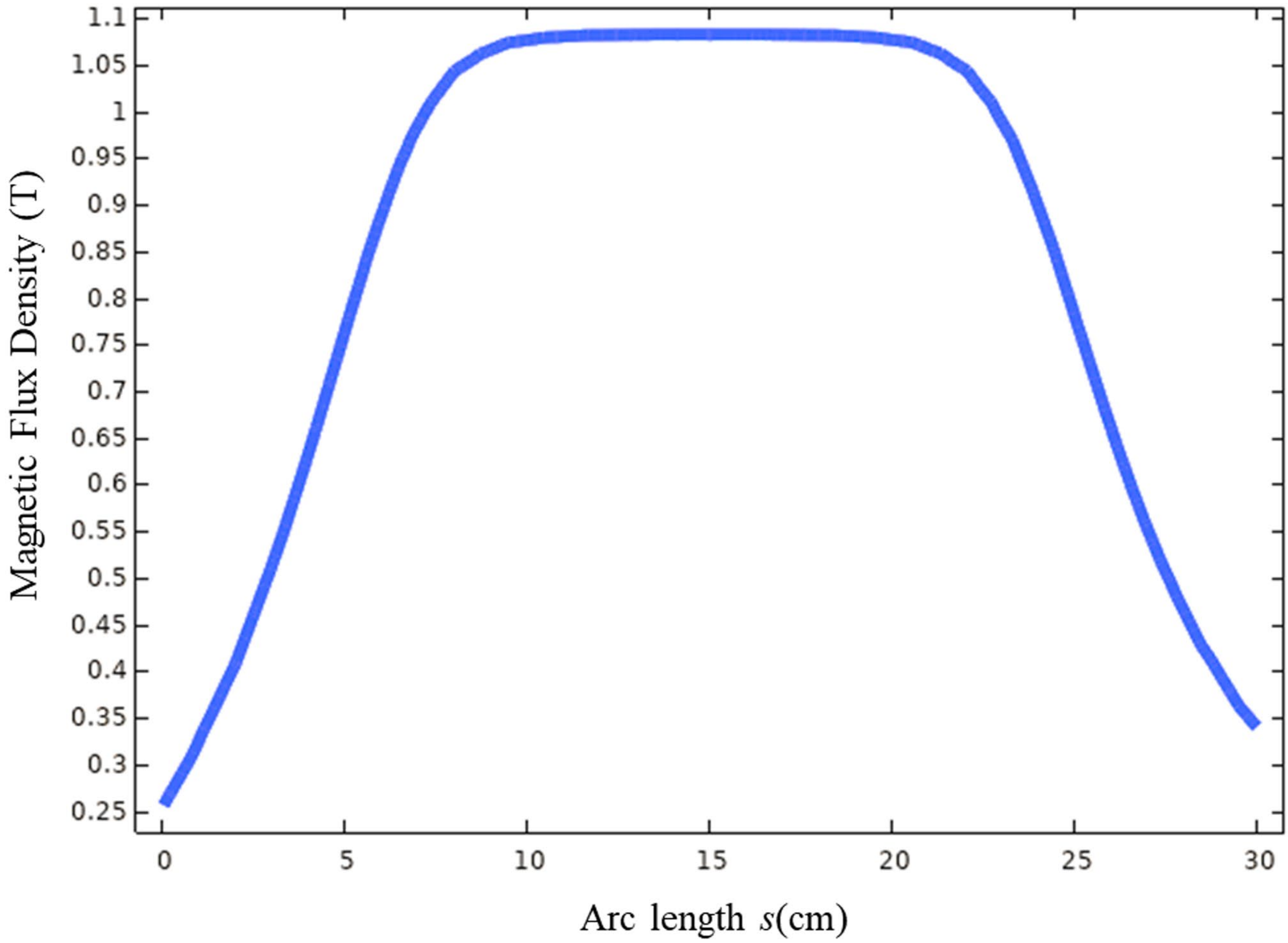

Fig. 5. Simulated magnetic flux density distribution in the C-type dipole dump magnet, showing fringe-field formation and field decay at the entrance and exit.

As shown in Fig. 6, the excitation current required by the C-type dipole dump magnet increases linearly with electron kinetic energy. The experimental data are well described by a linear fit

$$I = 1.1093 + 0.5921\,E,$$

with a coefficient of determination of $R^2 = 0.9957$, indicating excellent linearity. Measurement uncertainties originate primarily from Hall probe calibration, probe positioning, and power-supply current stability, and are shown as error bars in Fig. 7.

In the design workflow, two-dimensional FEM (2D FEM) analyses were used for rapid parametric optimization, while three-dimensional FEM (3D FEM) analyses were employed for final validation. The 2D model, based on a mid-plane cross-section, accurately represents the magnetic field in the central region but neglects longitudinal end effects. In contrast, the 3D model includes the full magnet geometry, accounting for fringe fields, flux leakage, and geometric asymmetries, which are critical for dump magnet applications. A direct comparison (Fig. 8) shows that while central field values agree well, the 3D model predicts a reduced effective magnetic length due to end effects, which is essential for accurate beam-deflection calculations.

The electromagnetic performance of the C-type dipole dump magnet was further evaluated by analyzing key operating parameters, including electron kinetic energy, excitation current, operating voltage, electrical resistance, magnetic field strength, thermal load, and maximum achievable field. These results are summarized in Table 2. Nominal magnetic field values and bending angles were calculated using analytical beam-optics relations, while all other quantities, including effective magnetic lengths and fringe-field-related parameters, were obtained from 3D FEM simulations under nominal excitation currents and ideal alignment conditions. The underlying assumptions, calculation methods, and relevant formulas are detailed in the section "Magnetic field simulation and effective length".

Radiation-induced energy deposition obtained from Monte Carlo simulations was mapped onto the magnet geometry as volumetric heat sources and combined with resistive heating in COMSOL Multiphysics to perform a steady-state electromagnetic–thermal analysis. The resulting thermal load led to a maximum coil temperature rise of 18.7 °C above ambient, indicating that safe air-cooled operation is feasible without the need for water-

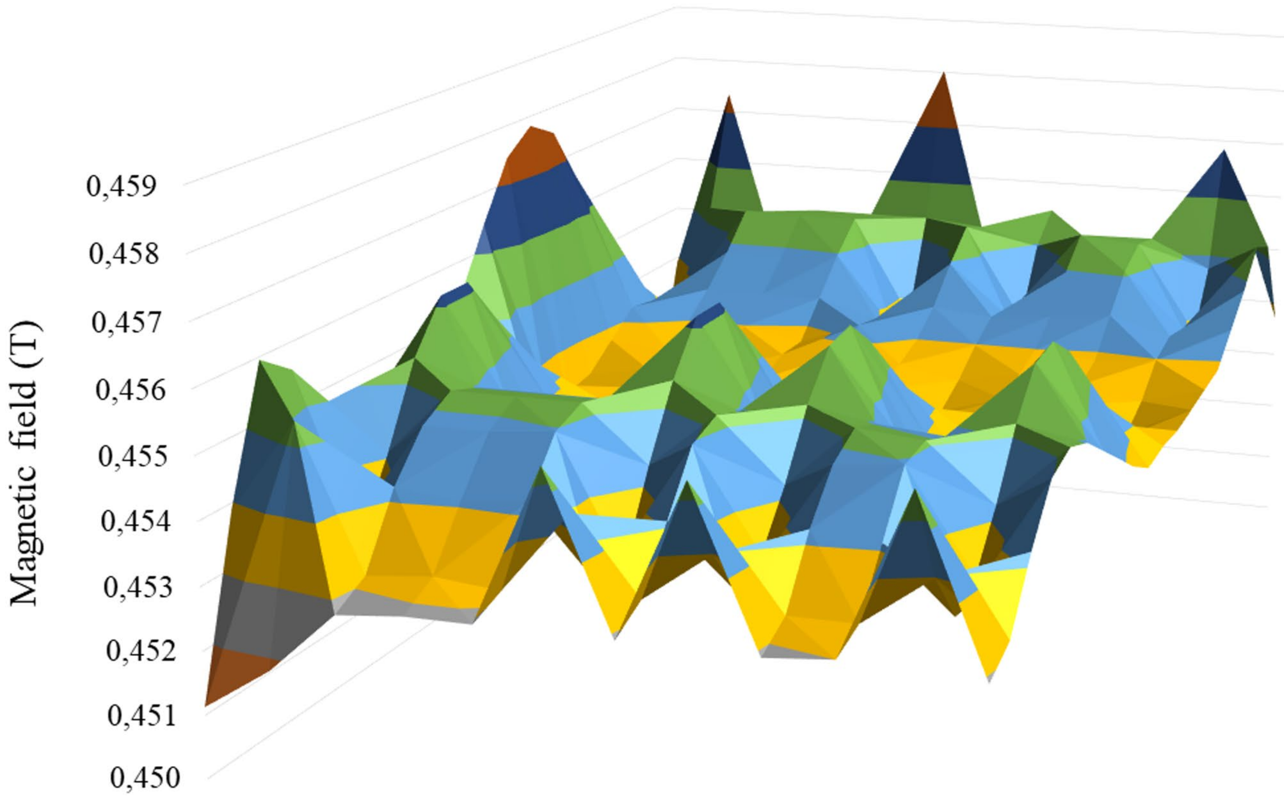

Fig. 6. Spatial distribution of the magnetic field at 40 MeV operation.

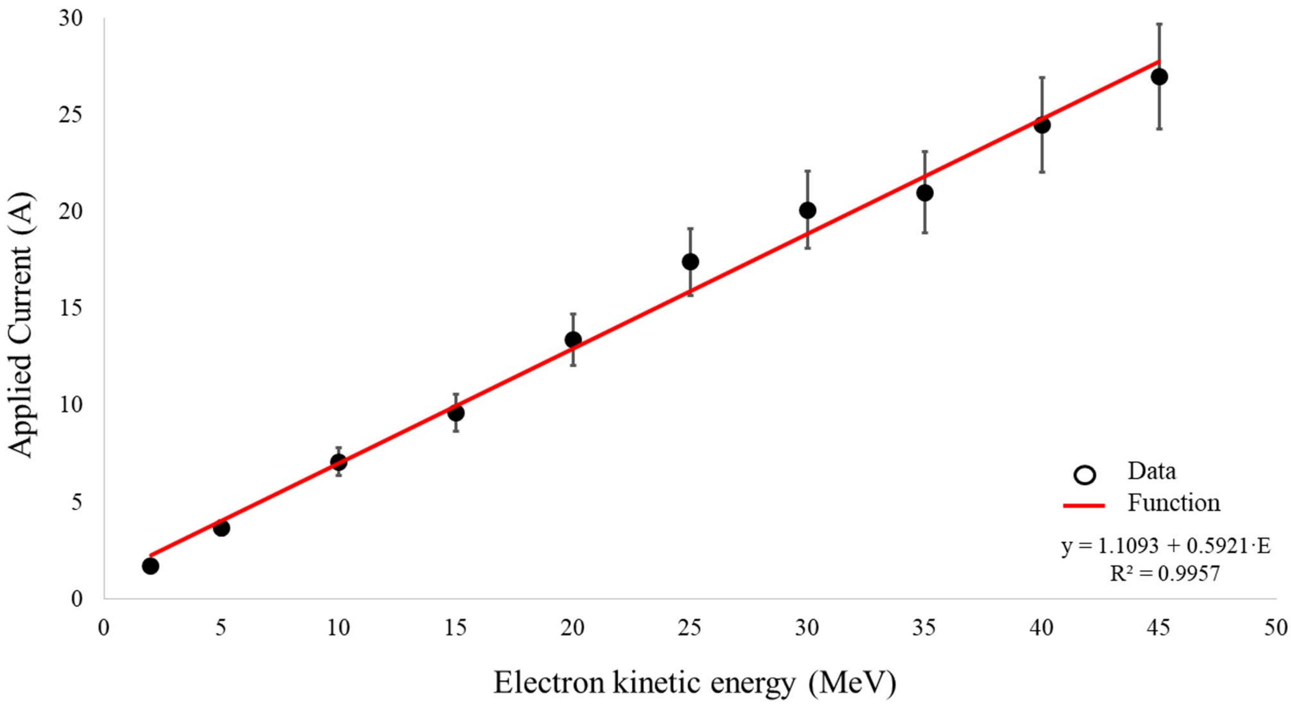

Fig. 7. Optimal applied current versus electron kinetic energy for 42° beam deflection.

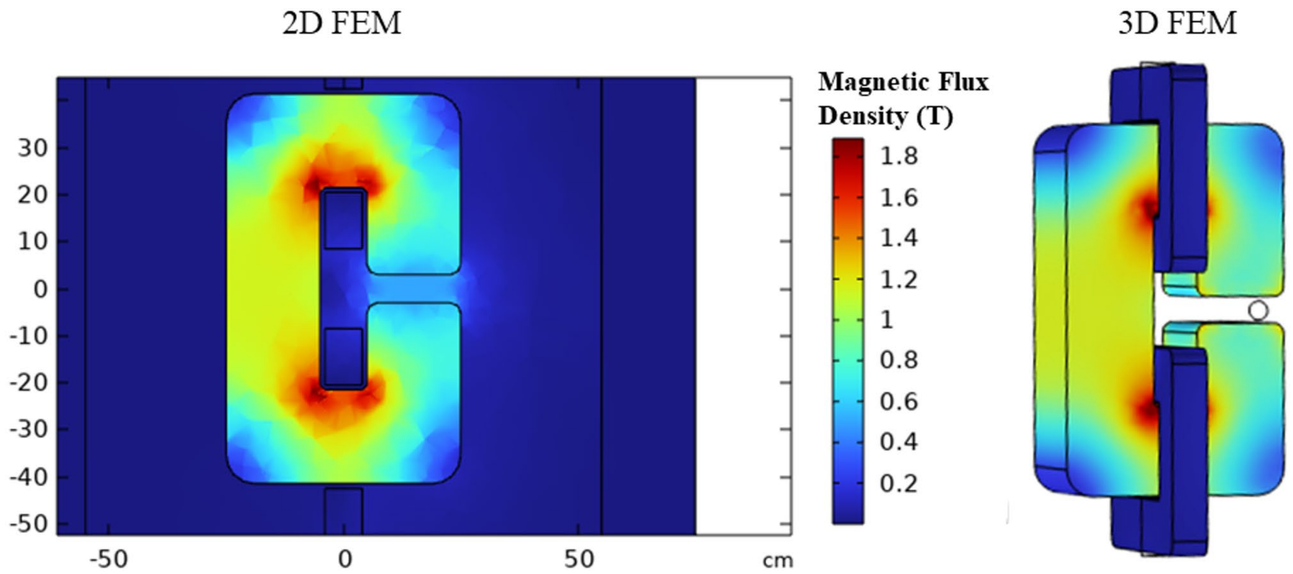

Fig. 8. Magnetic flux density variation of the C-type dipole dump magnet from 3D and 2D FEM analyses.

Electron Kinetic Energy, E_k	Applied Current Value	Voltage	Resistance	Magnetic Field Strength, B_0	Generated Heat	Maximum Magnetic Field
(MeV)	(A)	(Volt)	(Ω)	(T)	(W)	(T)
2	1.7	1.30	1.53	0.0316	1.1	0.200
5	3.7	2.84	1.53	0.0689	5.2	0.654
10	7.1	5.45	1.53	0.1320	19.3	0.841
15	9.6	7.36	1.53	0.1790	35.3	0.946
20	13.4	10.28	1.53	0.2500	56.3	1.053
25	17.4	13.34	1.53	0.3240	116.0	1.320
30	20.1	15.41	1.53	0.3750	154.0	1.440
35	21.0	16.10	1.53	0.3910	169.0	1.560
40	24.5	18.75	1.53	0.4570	230.0	1.800
45	27.0	20.55	1.52	0.6500	277.0	1.947

Table 2. Operating parameters and performance characteristics of the C-type dipole dump magnet.

cooling or cryogenic systems. The highest temperatures were observed near the beam-facing side of the iron yoke and in the front sections of the aluminum coils, consistent with the neutron dose distribution. Thermal imaging measurements validated the numerical predictions, indicating a maximum temperature rise of 18.9 °C above ambient (Fig. 9). At a laboratory ambient temperature of 23.4 °C, the peak coil temperature reached 42.3 °C. Measurements were carried out using a Fluke Ti125 infrared camera (temperature accuracy: ±2% or ± 2 °C). The highest temperatures were observed on the aluminum coils, while the temperature increase in the iron core remained comparatively low. These results are in good agreement with the simulated heat distribution and confirm the reliability of the coupled electromagnetic–thermal analysis.

To further limit the temperature rise, the coils were implemented in a parallel rather than a series configuration, in which the total magnet current is distributed among multiple coil paths. This reduced the effective electrical resistance by approximately a factor of four and correspondingly lowered Joule heating, thereby providing a comfortable thermal margin and contributing to the thermal stability and reliable operation of the magnet. In contrast, a series winding configuration would be expected to produce substantially higher Joule heating and a much larger temperature rise, potentially approaching the upper bounds of safe operation for air-cooled coils. Given the fringe-field-dominated geometry and the resulting large effective magnetic length, resistive losses become a dominant thermal constraint, making the parallel winding scheme essential for maintaining reliable air-cooled operation.

Particle radiation analysis

Radiation transport and neutron production analyses were performed using Monte Carlo simulations implemented with the MCNP 6.2 code[18]. The simulations employed detailed three-dimensional geometry models of the C-type dump magnet, the neutron shielding materials, and the surrounding structures, together with realistic beam source definitions representative of TARLA MIR/THz FEL operating conditions. The same

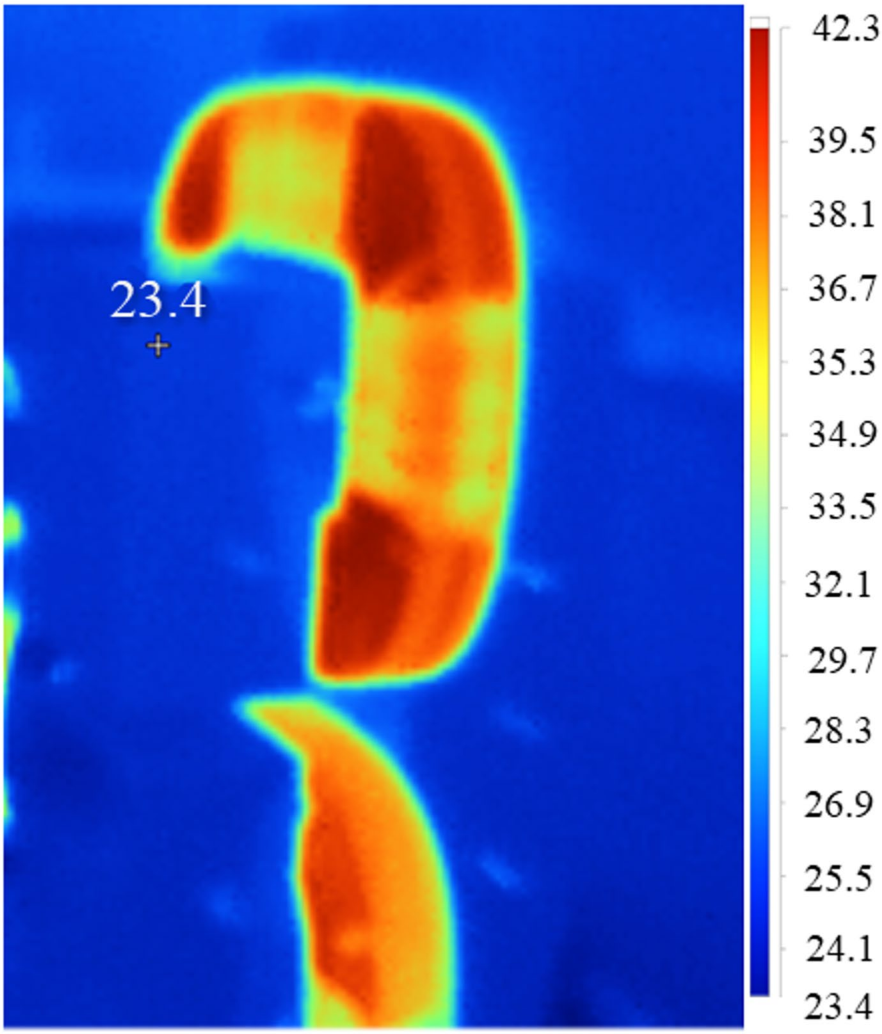

Fig. 9. Infrared thermographic image of the magnet under steady-state operation at 40 MeV.

material compositions used in the COMSOL simulations were also adopted in the MCNP models to ensure consistency between the electromagnetic–thermal and radiation transport analyses.

The Monte Carlo method was chosen for its effectiveness in modeling stochastic particle transport and interaction processes in matter, in which particle properties such as energy, direction, interaction mechanisms, energy loss, and scattering are governed by probabilistic distributions. A full-scale model of the dump magnet was employed, with the iron yoke subdivided into five regions in order to evaluate the spatial distribution of energy deposition using F6 energy-deposition tallies. The aluminum coils were modeled with a 1 cm air gap from the yoke, and both the yoke and coil volumes were discretized into cells to quantify regional energy deposition in units of MeV g^{-1}, as illustrated in Fig. 10. All simulations were carried out using 1×10^8 primary particles, providing sufficient statistical accuracy for the calculated neutron flux and energy deposition distributions.

Monte Carlo simulations show that the highest radiation-induced energy deposition occurs in cells 100 and 110 (Fig. 11), which correspond to the front region of the iron yoke facing the beam absorber. This clearly confirms the primary shielding role of the yoke against secondary radiation. The analysis of thermal, slow, and fast neutron components further indicates that the energy deposition in both the iron yoke and the aluminum coils increases with neutron energy, underscoring the need for dedicated neutron shielding to ensure long-term and stable magnet operation.

The radiation-induced energy deposition was calculated using Monte Carlo simulations and mapped onto the magnet geometry as volumetric heat sources. These were subsequently coupled with Joule heating from the coils in COMSOL Multiphysics to perform a steady-state electromagnetic–thermal analysis, enabling a realistic evaluation of temperature rise under operational radiation exposure.

The neutron shielding system was designed to provide comprehensive coverage along the dump region and is fully integrated with the magnet structure. Hydrogen-rich materials combined with boron-containing layers were employed to attenuate both fast and thermal neutrons. Localized shielding blocks were placed around regions of highest dose, particularly near the beam impact area, to minimize neutron streaming toward radiation-sensitive components. The shielding geometry was optimized to balance attenuation performance, mechanical

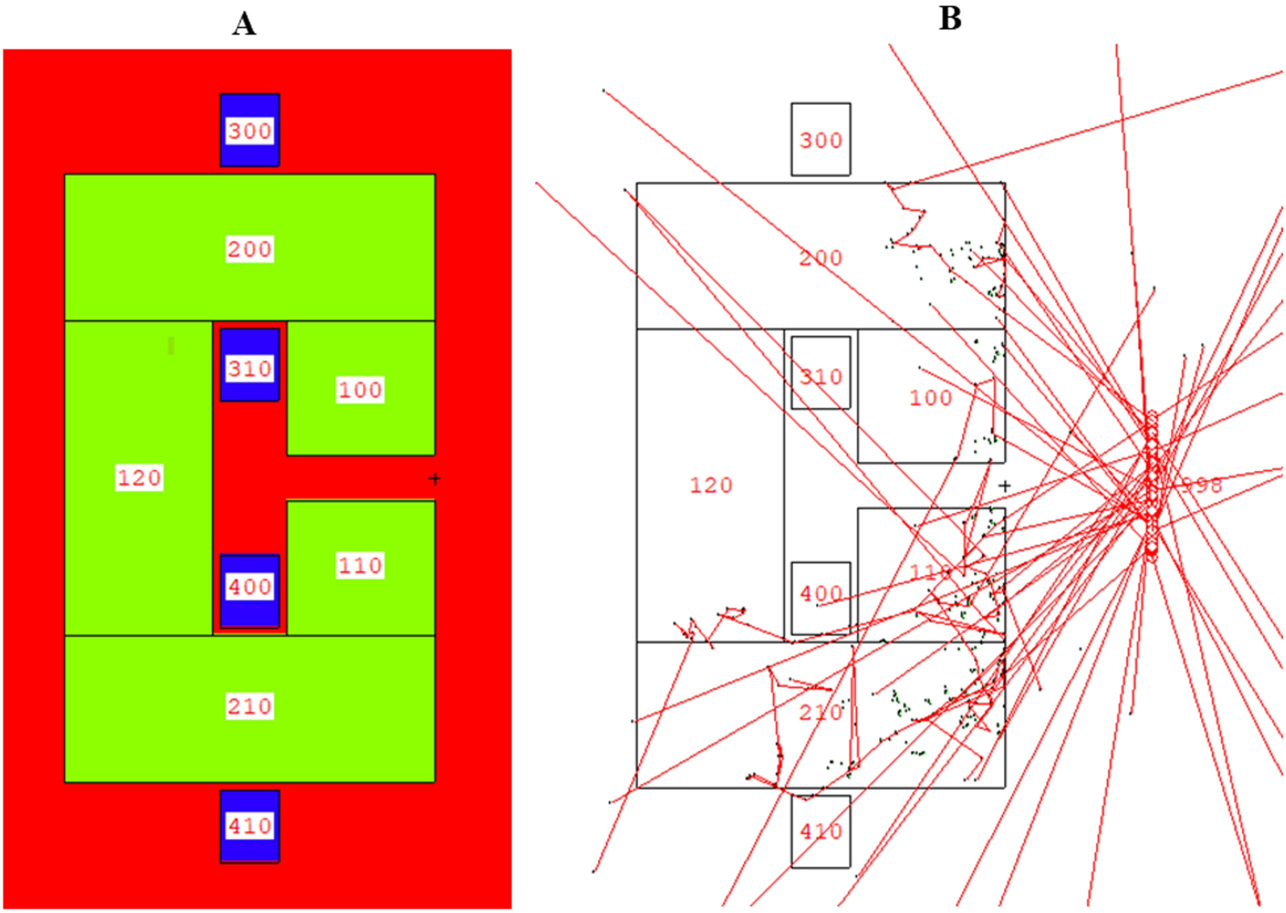

Fig. 10. **A** Simulation geometry in the XZ plane. **B** Trajectories (tracks) and interaction points of the first 50 particles at an electron kinetic energy of 40 MeV.

compatibility, and accessibility for installation and maintenance, with all shielding components mechanically integrated into the magnet yoke to ensure stable alignment during operation.

The combined effects of radiation heating and resistive losses resulted in a maximum coil temperature rise of 18.7 °C above ambient, confirming that safe air-cooled operation is achievable without the need for water-cooling or cryogenic systems. The highest thermal loads were observed near the beam-facing side of the iron yoke and in the front sections of the aluminum coils, in good agreement with the neutron dose distribution predicted by the Monte Carlo simulations.

Neutron shielding

Hydrogen-rich materials such as polyethylene, water, and paraffin are widely used for fast-neutron moderation, while boron-doped polymers and ^{10}B-containing compounds are commonly employed for thermal neutron absorption due to their high capture cross section[19]. Recent developments in neutron-shielding technology include gadolinium-doped composites, hydrogen-enriched concretes, and layered polyethylene–B_4C structures[20,21], as well as lightweight and thermally stable polymer-based shielding materials[22,23].

Neutron shielding relies on the combination of hydrogen-rich moderators and boron-containing absorbers, since high-density metals are largely ineffective for neutron attenuation. In this study, shielding measurements were performed for two candidate materials at 11 different thicknesses to achieve 99% neutron attenuation. The required thickness was determined to be 5 cm for Sample 1 (B_4C-based) and 6.95 cm for Sample 2, a newly developed composite. Owing to its local availability, lower cost, and scalability, Sample 2 was selected and implemented with a thickness of 7 cm.

A hybrid shielding composite was developed by incorporating B_4C and a high-boron compound into a hydrogen-rich epoxy matrix. The particle size distribution and resin ratio were optimized to maximize neutron attenuation while minimizing void formation. The innovative bor-rich powder-based hybrid shielding process described herein has been subject to a patent application, highlighting its novelty and proprietary methodology. The fabrication of the shielding layers represents the most innovative aspect of this work, employing a precise, stepwise procedure to maximize density and mechanical stability:

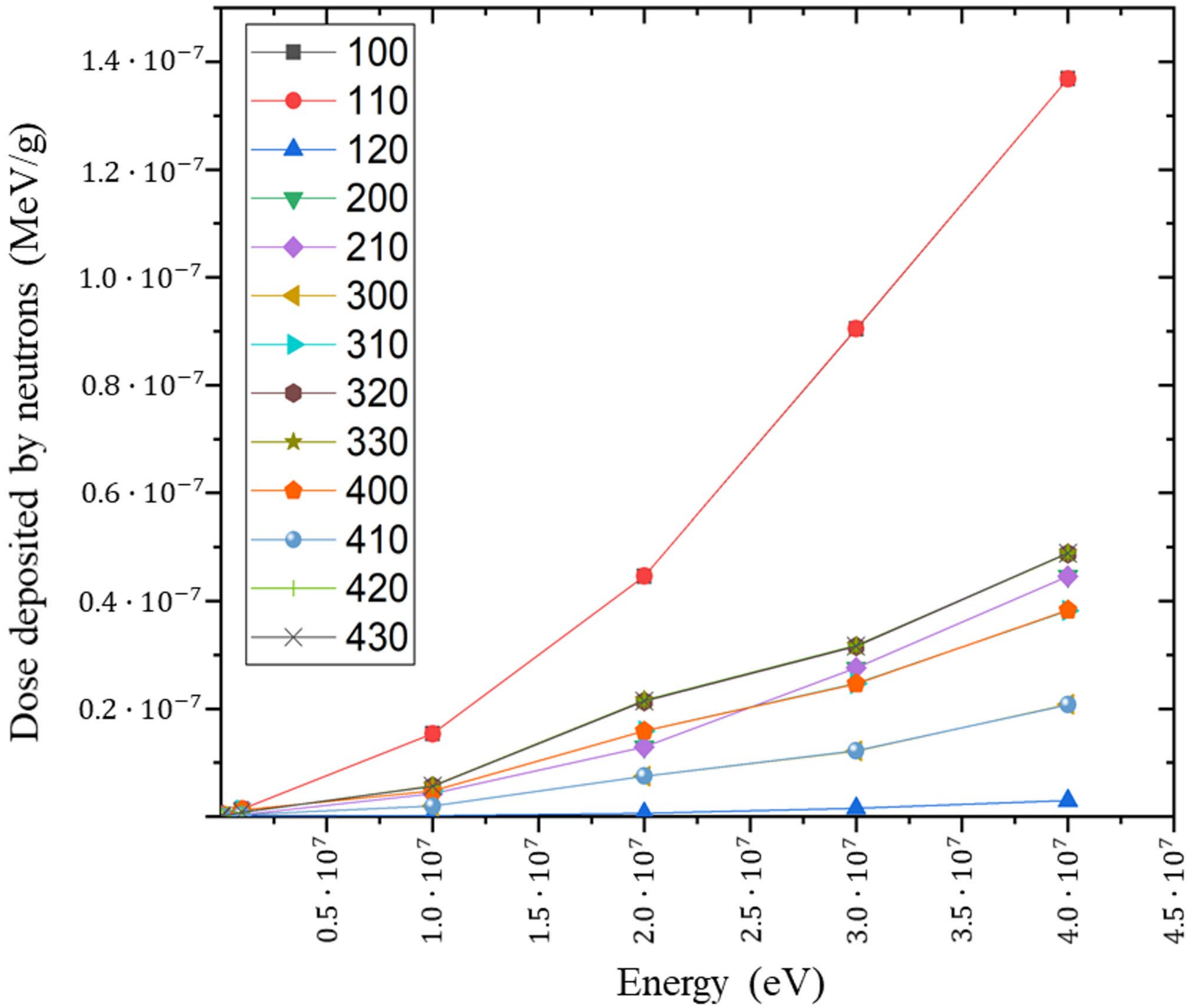

Fig. 11. Dose deposited in different cells by neutrons with 40 MeV.

- Raw Material Preparation: Bor-rich powder (purity ≥ 99.5%, particle size 45–90 μm) was selected and vacuum-dried at 90 °C for 8 h to remove residual moisture and ensure a uniform particle size distribution suitable for high-density compaction.
- Mold Preparation: Stainless steel or aluminum molds are coated with PTFE to facilitate demolding and ensure high surface quality.
- Powder Filling: The mold is filled with the amount of bor-rich powder required to achieve a theoretical density of 2.38–2.42 g/cm³.
- First Vacuum Stage: Vacuum is applied to < 0.01 mbar for 15 min to remove adsorbed gases and moisture and evacuate interparticle voids.
- Vibration Stage: Controlled mechanical vibration (50 Hz frequency, 3 mm amplitude, 50 min duration, continuous operation) compacts the powder, minimizing porosity and achieving > 95% theoretical density.
- Second Vacuum Stage: Vacuum is reapplied (< 0.01 mbar, 10 min) to evacuate microvoids generated during vibration and finalize densification.
- Demolding: The block is slowly removed using a hydraulic press at 0.5 mm/s to preserve integrity and prevent cracking.
- Final Drying / Thermal Treatment: Heat treatment at 120 °C for 24 h ensures physical densification without chemical bonding and improves mechanical strength.
- Surface Machining: CNC milling produces the precise magnetic geometry, ensuring dimensional tolerances and surface quality.

Prototype samples were tested at the TENMAK Büyükçekmece neutron facility, where both shielding efficiency and the spatial power distribution of the neutron source were characterized (Fig. 12).

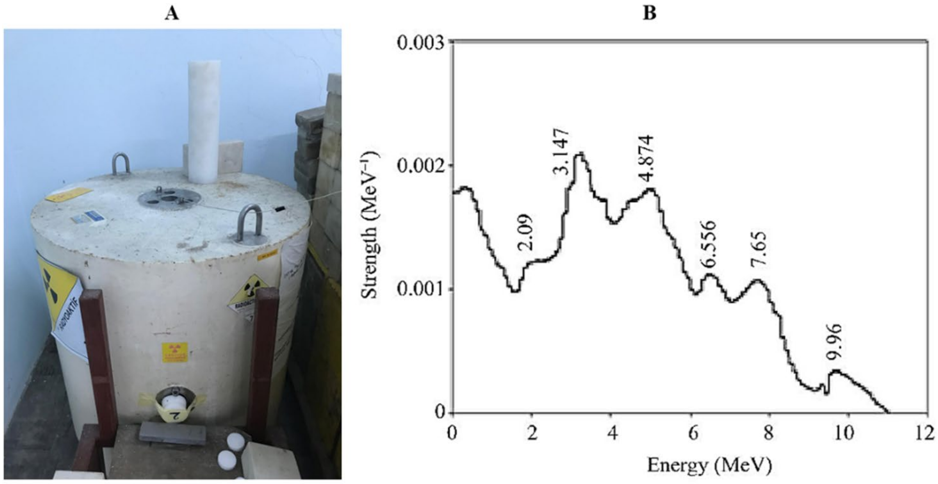

Fig. 12. **A** Schematic of the neutron test system and **B** spatial power distribution of the neutron source.

Feature	Conventional Dump Magnets	Proposed Design
Radiation-driven geometry	No	Yes
Coil separation	Limited	Optimized
Low-Cu steel	Rare	Used
Neutron shielding integration	External	Integrated

Table 3. Key differences between conventional dump magnet designs and the proposed radiation-driven configuration.

This approach provides a cost-effective and lightweight neutron-shielding solution based on domestically sourced materials, offering practical benefits for accelerator facilities and broader industrial applications. In conventional beam dump magnet implementations at accelerator facilities such as DESY, SLAC National Accelerator Laboratory, and CERN, the primary design criteria are typically magnetic field strength, beam steering accuracy, and mechanical robustness. Radiation effects are generally addressed at later stages through external shielding or operational constraints rather than being integrated as a core design parameter. In contrast, the proposed dump magnet for the TARLA facility adopts a radiation-driven design methodology from the earliest conceptual phase. The main distinctions and improvements can be summarized as follows:

1. Radiation-Oriented Geometry Optimization: The magnet cross-section and pole configuration were optimized not only for magnetic field uniformity but also to minimize direct radiation exposure to sensitive regions, particularly the coil windings.
2. Coil Displacement from Primary Radiation Line: Unlike conventional C-type dipole layouts where coils are relatively close to the beam interaction region, the present design deliberately repositions and partially shields the coils, significantly reducing neutron and gamma flux deposition in insulating materials.
3. Low-Copper, High-Iron Electrical Steel Selection: Material selection was guided by activation and radiation-damage considerations. The use of low-Cu, high-Fe electrical steel reduces long-term activation and mitigates radiation-induced degradation compared to standard construction steels.
4. Integrated Neutron Shielding Concept: Rather than employing standalone shielding blocks external to the magnet body, hydrogen-rich and boron-containing materials were incorporated directly into the magnet assembly. This integrated approach enhances fast and thermal neutron attenuation while maintaining compactness.
5. Coupled Monte Carlo–FEM Design Workflow: Radiation transport simulations (Monte Carlo) were directly coupled with electromagnetic and thermal finite-element analyses. This allows quantitative evaluation of radiation-induced heat loads and material stress, enabling predictive lifetime assessment—an aspect often absent in traditional dump magnet designs.

The proposed design provides improved radiation tolerance, reduced activation, enhanced operational reliability, and potentially longer service life under continuous FEL operation conditions. These features make it particularly suitable for medium-energy MIR/THz FEL facilities where beam losses and dump-induced radiation fields can significantly impact magnet integrity over time. A comparative summary highlighting the key differences between conventional dump magnet designs and the proposed radiation-driven configuration is provided in Table 3.

Fig. 13. Schematic illustration of the neutron shielding fabrication process before and after curing.

Shield Thickness	Neutron Shielding Efficiency Sample I	Sample II
(cm)	(%)	(%)
2.5	92.3	83.0
2.6	93.4	84.2
3.0	95.2	87.9
3.5	96.9	91.0
3.6	97.2	91.6
3.8	97.6	92.7
4.0	97.9	93.7
4.5	98.6	95.4
5.0	99.0	96.6
6.0	99.6	98.2
7.0	99.8	99.1

Table 4. Effect of shield thickness on neutron attenuation efficiency.

Figure 13 shows the Schematic illustration of the neutron-shielding fabrication process before and after curing, showing the material composition, shaping procedure, and the structural consolidation achieved after curing.

Three independent measurements were performed for each of the two shielding samples at 11 different thicknesses, and the average values were used in the analysis. Repeated measurements were carried out to improve measurement accuracy and reduce experimental uncertainty. The resulting attenuation data are summarized in Tables 4 and 5.

	Shield Thickness (cm)	Measurement				Neutron Shielding Efficiency (%)
		First	Second	Third	Average	
Reference (Empty)	-	2386	2292	2425	2367.7	-
Sample I	2.6	149	164	158	157.0	93.4
Sample II	3.8	176	171	172	173.0	92.7

Table 5. Experimentally measured neutron shielding efficiencies for the tested materials.

Results

This study reports the design, simulation, and experimental validation of a radiation-resistant C-type dipole dump magnet developed for MIR/THz FEL applications at the TARLA facility. The approach integrates material characterization, electromagnetic modeling, radiation analysis, and neutron-shielding experiments to evaluate system performance under realistic operational conditions. Magnetic core materials were screened using X-ray fluorescence (XRF) and vibrating sample magnetometer (VSM) measurements to assess elemental composition and magnetic properties. Electrical steel was selected based on its high iron content, low copper concentration, and the absence of activation-prone elements. The experimentally measured B–H curve exhibits a rapid increase in magnetic flux density at low magnetizing fields, followed by a gradual approach to saturation. This measured magnetization behavior was implemented in COMSOL Multiphysics[24], yielding a maximum deviation of 6.28% between simulated and experimental values near saturation.

The magnet features a 60 mm pole gap to deflect electron beams in the 2–45 MeV energy range by a bending angle of 42°. Aluminum conductors were employed to minimize long-term activation, with 448 turns per pole producing a maximum magnetic field of 0.65 T at an operating current of 27 A. A hierarchical simulation strategy was adopted, using 2D finite-element analysis for parametric optimization and 3D simulations for final validation of fringe fields and end effects. The calculated magnetic field of 0.4570 T corresponds to a relative difference of 0.59%, confirming excellent agreement between simulation and experimental results.

Radiation effects were evaluated using Monte Carlo simulations with 1×10^8 primary particles. Energy deposition is concentrated primarily on the inner surfaces of the iron yoke and adjacent coil regions. Neutron-shielding measurements were conducted for two hydrogen-rich, boron-containing materials at multiple thicknesses. A B_4C-based material achieved 99% neutron attenuation at a thickness of 5 cm, while a newly developed composite material achieved comparable attenuation at 6.95 cm.

The key improvement of the proposed design lies in shifting from a field-performance-driven approach to a radiation-resilience-driven magnet design philosophy, where radiation transport, shielding, material activation, and thermal effects are treated as primary design parameters rather than secondary corrections.

Discussion

This study demonstrates the successful design, simulation, and experimental validation of a radiation-resistant C-type dipole dump magnet for MIR/THz FEL applications at TARLA. A radiation-driven design methodology was adopted, integrating material selection informed by radiation effects, conservative magnetic design margins, finite-element modeling, Monte Carlo radiation simulations, and experimental measurements.

The close agreement between simulated and experimental magnetic field values, with deviations below 1%, confirms the validity of the electromagnetic modeling approach and the use of experimentally measured material properties. The conservative magnetic length margin ensures reliable beam interception under the influence of fringe fields, alignment tolerances, and radiation-induced uncertainties.

Radiation analysis revealed localized energy deposition in the inner yoke and coil regions, necessitating dedicated neutron shielding. A locally developed composite material was implemented due to its favorable attenuation performance, cost efficiency, and scalability, achieving the required neutron attenuation at a thickness of 7 cm. Experimental validation confirmed the predicted shielding performance.

The realization of a fully functional, radiation-resilient dump magnet demonstrates the robustness of the proposed design strategy. The methodology and experimental findings provide a practical, transferable reference for the development of compact, radiation-tolerant beam dump systems in FEL and similar accelerator facilities.

Conclusion

A radiation-resistant C-type dipole dump magnet has been designed and evaluated for MIR/THz FEL applications at TARLA. The design integrates radiation-driven considerations from the earliest conceptual stage, including geometry optimization, coil shielding, low-Cu high-Fe electrical steel selection, and incorporation of neutron-attenuating materials.

Electromagnetic performance, magnetic field distribution, and thermal behavior were analyzed using 3D finite-element simulations, while material properties were experimentally characterized using VSM and XRF analyses. Comparison between experimental and simulation data demonstrated good agreement, consistent with expected engineering tolerances.

Monte Carlo simulations provided insights into radiation fluxes and heat deposition, enabling optimization of the neutron shielding layout. The proposed design achieves improved radiation tolerance, reduced activation, and reliable operational performance under expected FEL beam conditions without requiring complex cooling or cryogenic systems.

The developed dump magnet provides a reference approach for similar medium-energy FEL and linac facilities, demonstrating that early integration of radiation considerations into magnet design can significantly enhance lifetime and operational reliability. Future work may focus on experimental validation under beam operation and further optimization of shielding materials and geometries.

Data availability

The data supporting the findings of this study are available from the corresponding author upon reasonable request.

Received: 27 December 2025; Accepted: 18 March 2026
Published online: 24 March 2026

References

1. Tanaka, K. High intensity beam handling for nuclear and particle physics. *Nucl. Instrum. Methods Phys. Res., Sect. B*. **317**, 381–384. https://doi.org/10.1016/j.nimb.2013.05.059 (2013).
2. Mühle, C. et al. *Radiation resistant prototype dipole for the first stage of Super-FRS (GSI Report)* (GSI Helmholtzzentrum für Schwerionenforschung GmbH, 2012).
3. Leibrock, H. et al. Radiation resistant magnets for the Super-FRS of the FAIR project. *In Proceedings of the IEEE* (radiation-related magnet sessions) (2020).
4. Kahn, S. A., Dudas, A., Flanagan, G. & Gupta, R. C. Thermal-mechanical analysis of the FRIB nuclear fragment separator dipole magnet. In Proceedings of the 6th International Particle Accelerator Conference (IPAC2015) (Paper WEPTY064). JACoW. https://doi.org/10.18429/JACoW-IPAC2015-WEPTY064 (2015).
5. Zeller, A. F., DeKamp, J. C. & DeLauter, J. A radiation resistant dipole. *IEEE Trans. Appl. Supercond.* **15** (2), 1234–1237 (2005).
6. Takahashi, H. et al. Indirectly Cooled Radiation-Resistant Magnets for Hadron Target Station at J-PARC. *IEEE Trans. Appl. Superconductivity*. **20** (3), 344–347. https://doi.org/10.1109/TASC.2009.2038930 (2010).
7. Pepitone, K. et al. Design and Fabrication of a Canted-Cosine-Theta Double Aperture Orbit Corrector Dipole for the LHC. *IEEE Trans. Appl. Superconductivity*. **33** (5), 1–5. https://doi.org/10.1109/TASC.2023.3241571 (2023).
8. Mayer, M., Castronuovo, F., Jansson, U. & Fox, D. Steel tape-wound cut cores as magnet yokes for the beam-dump kickers of the Large Hadron Collider. *IEEE Trans. Magn.* **40** (4), 3051–3053 (2004).
9. Stein, W. RIA fragmentation line beam dump. In *Proceedings of the IEEE Particle Accelerator Conference* (PAC 2003), 2566–2568 (2003). https://doi.org/10.1109/PAC.2003.1289905
10. Trubacova, P. et al. Design strategies for beam impedance reduction of kicker magnets in particle accelerators. *IEEE Trans. Appl. Supercond.* **36**, 4100505. https://doi.org/10.1109/TASC.2025.3627179 (2026).
11. Mariotto, S., Busatto, S., Calzolaio, C., Rossi, L. & Sanfilippo, S. Sorti Study of HTS Energy-Saving Superconducting Magnet Options for the PSI Particle Beam Lines. *IEEE Trans. Appl. Superconductivity*. **35** (5), 1–5. https://doi.org/10.1109/TASC.2025.3543325 (2025).
12. Cao, D., Zhang, D., Kolar, J. W. & Huber, J. Conceptualization of a cryogenic 250-A power supply for high-temperature superconducting (HTS) magnets of future particle accelerators. In *Proceedings of the 11th International Conference on Power Electronics* (ICPE-ECCE Asia 2023), 688–696 (2023).
13. Garg, T. et al. High-field flux jump instabilities in cables for accelerator or compact fusion magnets and their effective suppression. *Sci. Rep.* **15**, 40782. https://doi.org/10.1038/s41598-025-24605-4 (2025).
14. Jenkins, R. & de Vries, J. L. *Practical X-ray Spectrometry,* 2nd edn (Springer, 1970).
15. Foner, S. Versatile and Sensitive Vibrating—Sample Magnetometer. *Rev. Sci. Instrum.* **30**, 548. https://doi.org/10.1063/1.1716679 (1959).
16. Wille, K. *The Physics of Particle Accelerators: An Introduction* (Clarendon, 2000).
17. Zickler, T. Basic Design and Engineering of Normal Conducting Iron-Dominated Electromagnets. *arXiv* arXiv:1103.1119 (2011).
18. MCNP — Monte Carlo N-Particle Transport & Code Version 6.2, Los Alamos National Laboratory, Los Alamos, NM, USA (2018).
19. Wang, K. et al. Recent Progress in Gd-Containing Materials for Neutron Shielding Applications: A Review. *Materials* **16** (12), 4305. https://doi.org/10.3390/ma16124305 (2023).
20. DiJulio, D. D. et al. A polyethylene-B4C based concrete for enhanced neutron shielding at neutron research facilities. Nuclear Instruments and Methods in Physics Research Section A: Accelerators, Spectrometers. *Detectors Assoc. Equip.* **859**, 41–46 (2017).
21. Toyen, D., Wimolmala, E., Hemvichian, K., Lertsarawut, P. & Saenboonruang, K. Highly Efficient and Eco-Friendly Thermal-Neutron-Shielding Materials Based on Recycled High-Density Polyethylene and Gadolinium Oxide Composites. *Polymers* **16** (8), 1139. https://doi.org/10.3390/polym16081139 (2024).
22. Hao, Z., Gong, J., Liang, C. & Polymer-Based Neutron Shielding Materials: A Critical Review on Application-Specific Performance Trade-Offs and Optimization Strategies. *Polym. Compos.* https://doi.org/10.1002/pc.70117 (2025).
23. Slimane Abdous, M., Derradji, Z., Mekhalif, K., Khiari, O. & Mehelli Younes Bourenane Cherif; Advances in Polymeric Neutron Shielding: The Role of Benzoxazine-h-BN Nanocomposites in Nuclear Protection. *Radiat. Res.* **200** (3), 242–255. https://doi.org/10.1667/RADE-23-00060.1 (2023).
24. COMSOL Multiphysics® v6.0. COMSOL AB, Stockholm, Sweden (2022).

Acknowledgements

This work was supported by The Scientific and Technological Research Council of Türkiye (TÜBİTAK) under Project No. 3231057, entitled "Development of a Radiation-Resistant C-Type Dipole Magnet for Accelerator Applications." The authors express their sincere gratitude to the research team at the Turkish Accelerator and Radiation Laboratory for their invaluable support and assistance in the construction of the magnet yoke. The authors also gratefully acknowledge the support of the Minister of Industry and Technology, Mr. Mehmet Fatih Kacır, for his encouragement and support of national manufacturing capabilities for accelerator technologies.

Author contributions

Z.O. conceptualized the study. Z.O., F.İ. and C.C. designed the methodology. S.Y., Ö.A. and M. Y. performed the simulations and data analysis. Z.O. wrote the original draft of the manuscript. K.B. and H. D. prepared the figures and tables. All authors reviewed and approved the final manuscript.

Funding
F.İ., Z.O., and C.C. received funding from the Scientific and Technological Research Council of Türkiye (TÜBİTAK) under Grant No. 3231057.

Declarations

Competing interests
The authors declare no competing interests.

Consent for publication
All authors have reviewed and approved the final manuscript for publication.

Additional information
Correspondence and requests for materials should be addressed to Z.O.